

Mitigating Radiation Loads in Nb_3Sn Quadrupoles for LHC Upgrades*

N.V. Mokhov and I.L. Rakhno
Fermilab, P.O. Box 500, Batavia, IL 60510

December 2, 2024

Abstract

Challenging beam-induced energy deposition issues are addressed for the next generation of the LHC high-luminosity interaction regions based on Nb_3Sn quadrupoles. Detailed MARS15 Monte Carlo energy deposition calculations are performed for various coil diameters, thicknesses and materials of the inner absorber at a field gradient of 200 T/m. It is shown that using the inner absorber made of tungsten-based materials can make the final focus superconducting quadrupoles compatible with a luminosity of $10^{35} \text{ cm}^{-2}\text{s}^{-1}$.

1 Introduction

The superconducting (SC) magnets of the Large Hadron Collider (LHC) under construction at CERN are based on $NbTi$ superconductor. The high-gradient quadrupoles for the interaction region (IR) inner triplets have been developed and manufactured by KEK and Fermilab [1]. These quadrupoles with 70-mm coils, provide a field gradient of 200 T/m and will allow one to achieve the nominal luminosity of $10^{34} \text{ cm}^{-2}\text{s}^{-1}$. As a result of thorough optimization of the IP1/IP5 layouts and low- β quadrupole design, the system was designed and built to protect the IR SC magnets against debris generated in the pp-collisions as well as to protect magnets and detectors against beam halo and a missteered beam coming to the IP. The system includes a set of absorbers in front of the inner triplet (TAS), inside the triplet aperture and between the low- β quadrupoles, inside the cryostats, in front of the D2 separation dipole (TAN), and between the outer triplet quads as well as a complex system in IP6 and tertiary TCT collimators for the incoming beam. Their parameters were optimized over the years in detailed energy deposition calculations at Fermilab to provide better protection consistent with the engineering constraints [2].

Several possible upgrade paths are under consideration to achieve a luminosity capability of $10^{35} \text{ cm}^{-2}\text{s}^{-1}$ at the LHC interaction points (IP) [3, 4]. Recent progress in the development of Nb_3Sn superconductor enables one to consider Nb_3Sn magnets as possible second generation quadrupoles for the LHC IRs [5]. The quadrupole fields sweep the secondary particles from pp-collisions at the IP into the SC coils along the vertical and horizontal planes, giving rise to a local peak power density ϵ_{max} that can substantially exceed the quench limits at such luminosity, with drastically reduced component lifetime and kW-level radiation loads on the inner triplet cryogenic system [6]. In several years of the LHC operations the magnets will have to be replaced with new quadrupoles which should provide the possibility of achieving the ultimate luminosity of $10^{35} \text{ cm}^{-2}\text{s}^{-1}$.

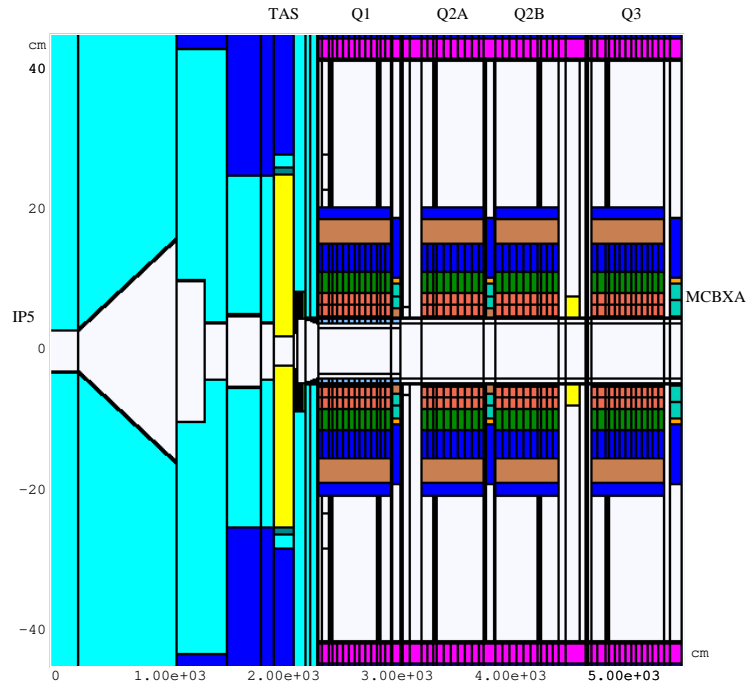
*Work supported by the Universities Research Association, Inc., under contract DE-AC02-76CH03000 with the U. S. Department of Energy.

This study is a continuation of our first look [7] at energy deposition issues for the new IR magnets. We address the dependence of radiation-induced energy deposition in the Nb_3Sn magnets on coil diameter, thickness and material of the inner absorber at a field gradient of 200 T/m by doing comprehensive energy deposition calculations with the MARS15 Monte Carlo code [8]. A configuration compatible with the luminosity of $10^{35} \text{ cm}^{-2}\text{s}^{-1}$ is proposed.

2 Inner Triplet Model

The calculation model of the IR is presented in Figs. 1-3. A longitudinal structure of the inner triplet region corresponds to the LHC lattice v6.5. The updates consist in replacing the quadrupoles based on $NbTi$ superconductor with larger bore ones based on Nb_3Sn . The four magnets in the region—Q1, Q2A, Q2B, and Q3—differ only in length while their radial structure, excluding the inner absorber (liner), is assumed to be the same. In this model, the baseline thickness of the liner is 6.2 mm in the region of Q1 quadrupole with no liner all the way downstream of Q1.

According to manufacturer’s specifications, the cold cable contains 50% bronze and 50% Nb_3Sn with a specific density of 5.4 g/cm^3 . A nominal field gradient of 200 T/m is used. A half crossing angle of $212 \mu\text{rad}$ and 21-mm TAS1 aperture were assumed in the calculations performed with the MARS15 Monte Carlo code [8]. Although some details of the model are specific to IP5 (horizontal crossing and detector-machine transition), results are applicable to both high-luminosity interaction regions, IP1 and IP5.



X
Z
Aspect Ratio: X:Z = 1:61.7222

Figure 1: Schematic view of the IP5 model with key elements labeled.

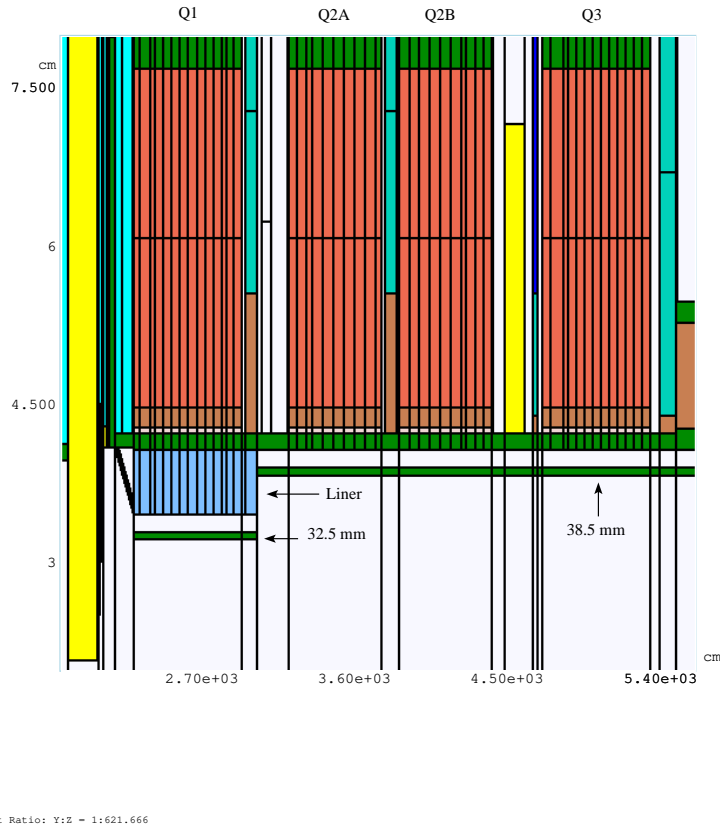


Figure 2: Fragment of the inner triplet geometry with a baseline liner.

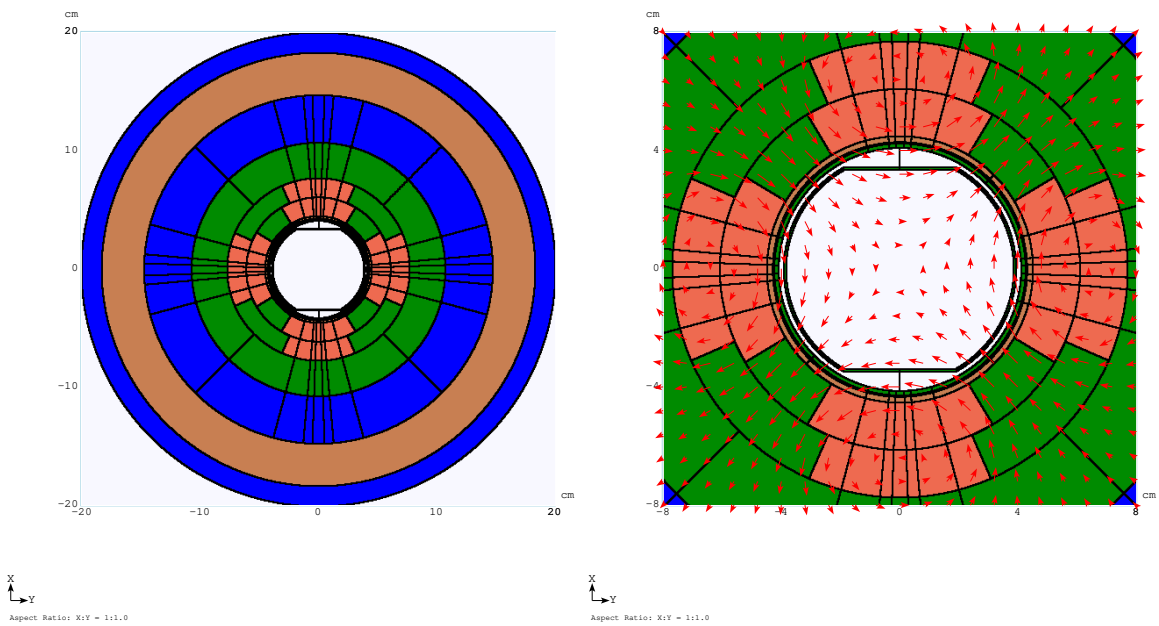


Figure 3: MARS15 geometry model of a 90-mm Nb_3Sn inner triplet quadrupole: cross section (left) and fragment showing more details as well as magnetic field distribution (right).

In this study we address the following two major problems relevant to beam-induced energy deposition in the LHC IR quadrupoles: peak power density and dynamic heat load. The former quantity enables one to determine if a magnet design under consideration is safe with respect to quenches. It is also directly related to the peak dose accumulated in the SC coils; this allows one to estimate their lifetime. The overall performance of the cooling system of the magnets should correspond to the heat load. The normalization of the data presented below corresponds to a luminosity of $10^{35} \text{ cm}^{-2}\text{s}^{-1}$. The design goal used below in connection with the peak power density has been calculated taking into account the quench limit for Nb_3Sn magnets of 5.0 mW/g [6, 9], with a safety factor of three on top of that [2]. It gives us 1.7 mW/g for the maximum power density in the SC coils as the design goal.

3 Peak Power Density in SC Coils

3.1 Coil aperture

A calculated distribution of peak power density, ϵ_{max} , in the inner triplet SC coils is shown in Fig. 4. Here a baseline stainless steel inner absorber is used. One can see that the peak power density exceeds the design goal significantly.

We have studied the dependence of ϵ_{max} on coil diameter. In our model developed for this purpose the radial position of each layer, including the beam screen, was adjusted appropriately while its thickness was kept the same (see Fig. 3). Due to lack of calculated magnetic field maps for coil diameters other than 90 mm, we apply a scaling procedure to the only existing field map. Namely, the two-dimensional distribution of the magnetic field developed previously for 90-mm Nb_3Sn magnets [10] is adjusted in the following way: given B_x and B_y for a two-dimensional grid $\{x_n, y_k\}$, we apply a multiplication correction factor of $D(mm)/90$, where D is inner coil diameter, to the coordinates of every single point of the grid as well as to the corresponding field components. Being an approximation the described procedure enables us to keep the field gradient constant.

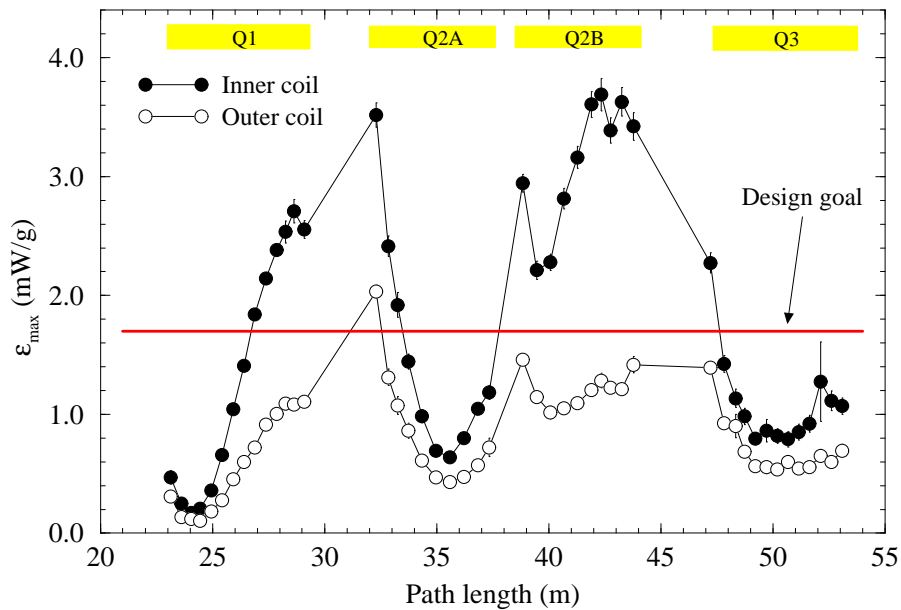


Figure 4: Distribution of peak power density along the inner triplet for 90-mm Nb_3Sn quadrupoles with a baseline stainless steel liner.

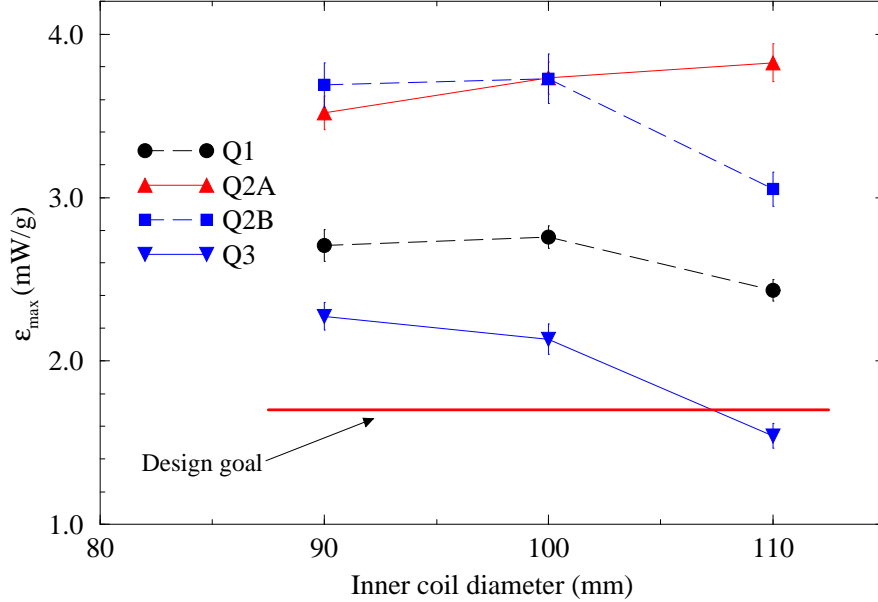


Figure 5: Distributions of maximum peak power density in the Nb_3Sn quadrupoles vs inner coil diameter calculated for a baseline stainless steel liner. The term 'maximum' refers here to the highest peak power density observed over a magnet length.

The calculated dependencies of maximum peak power density on coil diameter are shown in Fig. 5. One can see that at a fixed gradient, increasing the coil diameter from 90 to 110 mm one decreases ϵ_{max} in all the quadrupoles except Q2A, where ϵ_{max} is slightly up due to the reduced shielding effect of Q1. Power density is still unacceptably high. In order to understand qualitatively the dependencies shown in Fig. 5, we have examined partial energy deposition contributions to the hottest spot in the Q2B coil made by various shower components. A built-in tagging technique as well as histogramming [8] were used for this purpose. The analysis revealed that more than 90% of the total energy deposition at the hottest spot is due to electromagnetic showers induced by $\pi^0 \rightarrow 2\gamma$ decays (see also Sec. 3.4). The neutral pions are generated in inner regions of the system (beam screen, liner, cold bore) by charged hadrons coming from the IP. When increasing the coil diameter, two opposing factors come into play: (i) increased distance between the coil and beam gives rise to a reduction in energy deposited in the coil; (ii) to keep the same field gradient, one has to increase the magnetic field itself which, in turn, gives rise to an increase in charged hadron hit rate over the inner regions and, therefore, an increase in neutral pion production. The two factors acting together give rise to the distributions shown in Fig. 5.

3.2 Liner thickness

In order to reduce the peak power density in the quadrupoles, one can increase the inner absorber (liner) thickness d . A dependence of ϵ_{max} as a function of d has been calculated for 100-mm quadrupoles (see Fig. 6). For 90-mm ones there is not any extra room for the absorber from Q2A through Q3 because the beam screen is at 38.5 mm (see Fig. 2) and this is exactly the spatial limitation imposed by beam optics for $\beta^* = 0.25$ m [5]. For 100-mm quadrupoles one has the extra room to fit a liner up to 5 mm in thickness. One can see from Fig. 6 that even with a liner of increased thickness, ϵ_{max} in Q2B goes a bit beyond the design goal. Therefore, one has to rule this option out, at least for 90-mm and 100-mm quadrupoles.

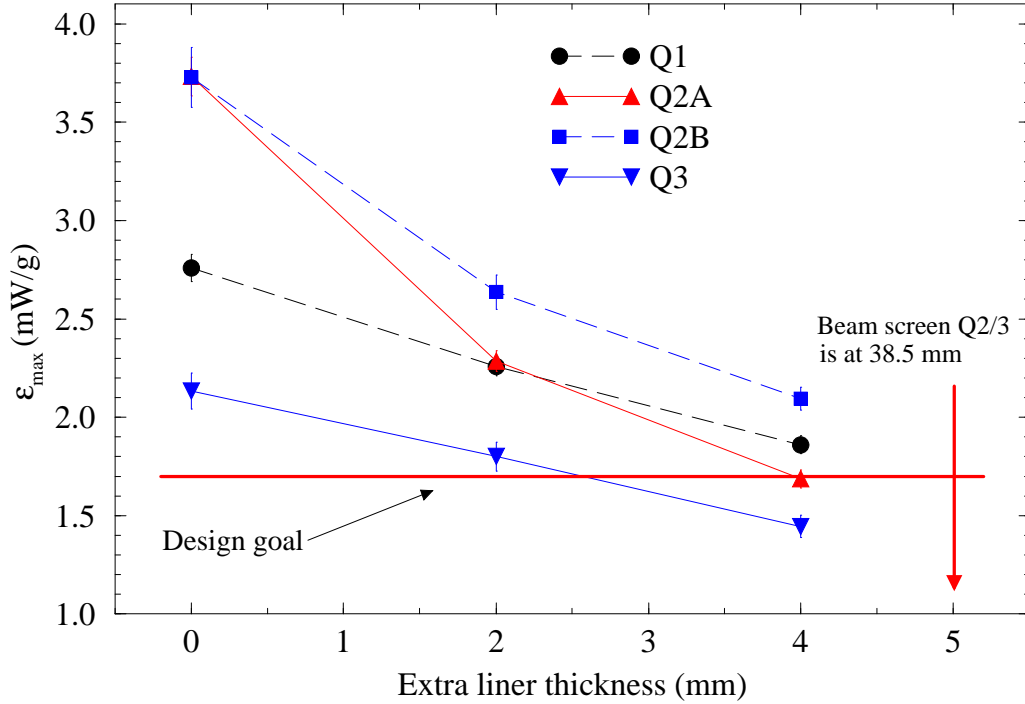


Figure 6: Peak power density in the Nb_3Sn quadrupoles with inner coil diameter of 100 mm vs extra thickness of the stainless steel liner, Δd . Total thickness of the liner, d , is equal to $d_0 + \Delta d$, where d_0 is the baseline liner thickness.

3.3 Spacers in SC coils

Another option that could help to reduce the peak power density in the coils is replacing the superconductor in the hottest spots along the entire magnet length with other material—a low- Z one. This has the advantage of providing decreased collision density and spreading the power density peak over a bigger volume. Aluminum and graphite were studied. A model and sample power density distribution are shown in Fig. 7. One can see that ϵ_{max} in the Q2B inner and outer SC coils is about 1.8 mW/g, slightly above the design goal.

One could further reduce the peak power density using the spacer approach by choosing one of the following options: (i) increasing the size of the spacers and extending them through the outer coil; (ii) using other material—more dense than aluminum; (iii) using a combination of the described aluminum spacers with a steel liner of increased thickness (see previous Section).

This approach has never been tested in practice. There are some difficulties with the coil design in this approach. It is also clear that there will be some effect on the field quality with the spacers, thus requiring magnet optimization studies. It seems that this approach could be considered as an auxiliary one that might be useful under other circumstances.

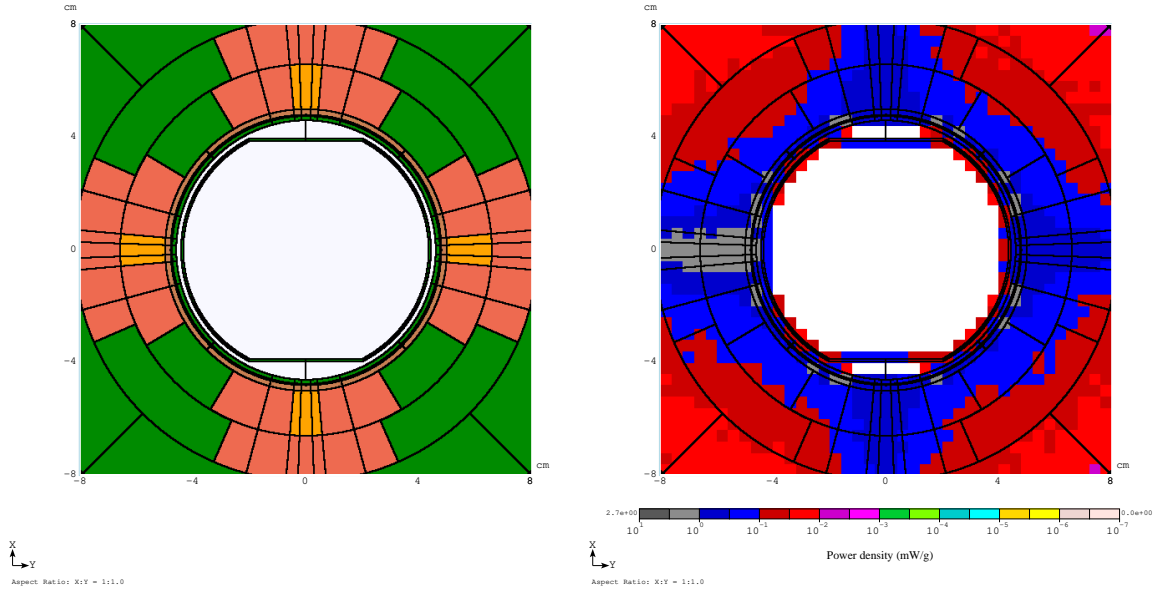


Figure 7: A cross section of the geometry model of a 100-mm Q2B quadrupole with spacers shown with brown color (left) and corresponding power density distribution around $Z = 42$ m calculated with aluminum spacers (right).

3.4 High-Z inner absorber

As described in Sec. 3.1, more than 90% of the energy deposition in the hottest spots of the SC coils is due to electromagnetic showers. Fig. 8 shows the energy spectra of electrons and photons for the hot spot in Q2B. One can see that about 50% of all photons in the region have energies from 200 to 400 keV. Therefore, a promising way to optimize the liner is to replace the stainless steel with a high- Z material. In such a case one can take the advantage of very strong photoabsorption that, at low energies, scales with the atomic number as $\sim Z^5$ (see Fig. 9). A good candidate is a commercially available tungsten-rhenium alloy, *W25 Re*, that contains 75% tungsten [12]. MARS15 calculations have revealed that, other things being equal, the *W25 Re* liner provides substantial absorption of low-energy photons and, therefore, a significant reduction of ϵ_{max} in all the quadrupoles (see Fig. 10). It should be noted that in our model the *W25 Re* is used to replace both the steel liner and the 1.5-mm steel cold bore adjacent to the liner (see Fig. 2). The design goal is reached with a *W25 Re* liner 7.2-mm thick in Q1 and 1-mm thick in the rest of the triplet.

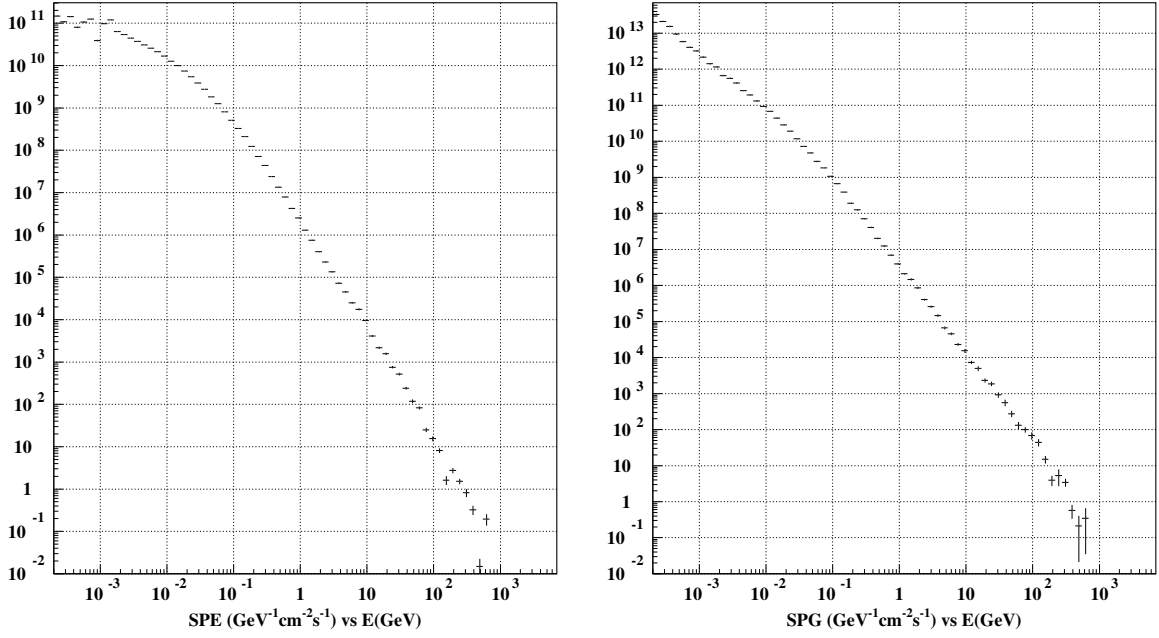


Figure 8: Energy spectra of electrons (left) and photons (right) averaged over the hottest spot in the inner Nb_3Sn coil of the Q2B magnet.

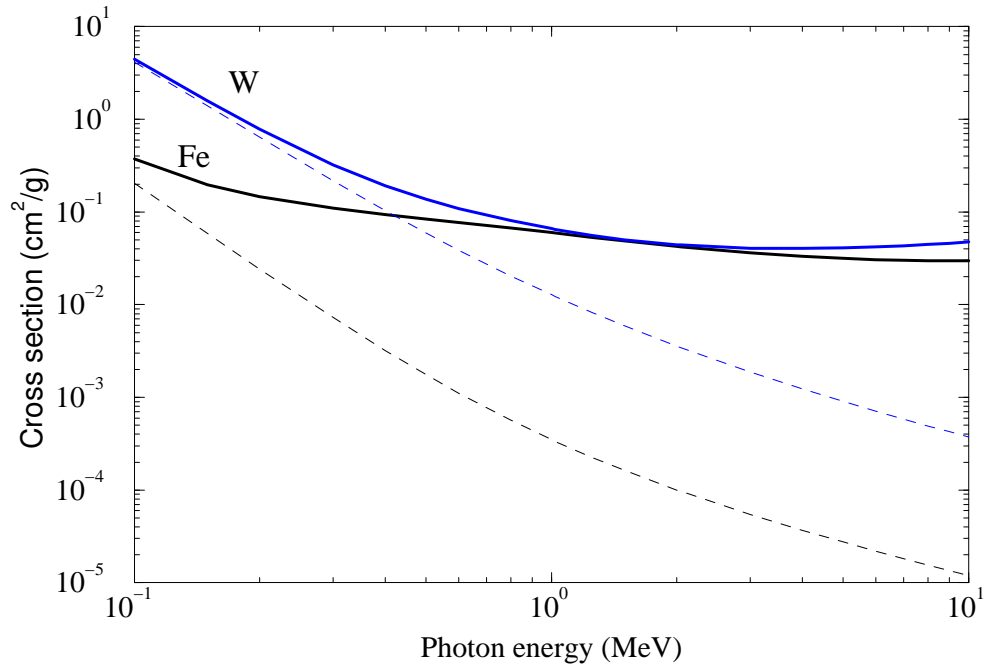


Figure 9: Photon total (solid) and photoabsorption (dashed) cross sections for iron and tungsten [11].

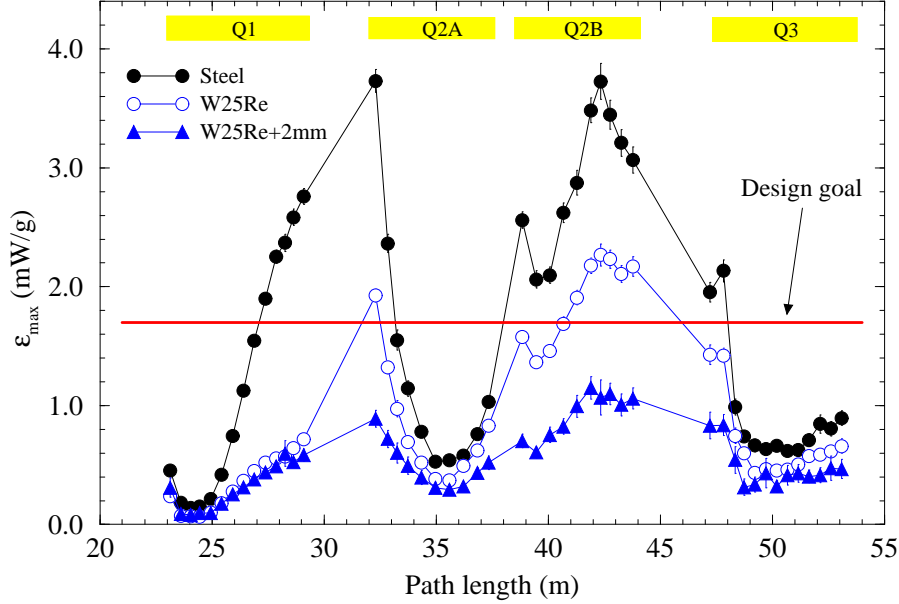


Figure 10: The peak power density in the inner coil of the 100-mm Nb_3Sn quadrupoles calculated for the baseline thickness of stainless steel, $W25 Re$ liners, and for a $W25 Re$ liner of increased thickness. $W25 Re$ is used to replace both the steel liner and 1.5-mm steel cold bore adjacent to the liner (see Fig. 2).

4 Dynamic Heat Loads

In order to design an adequate cooling system for the inner triplet at a luminosity of $10^{35} \text{ cm}^{-2}\text{s}^{-1}$, dynamic heat loads on the magnets are of primary importance. Results calculated for the liner and superconducting coils of the IR quadrupoles are shown in Fig. 11. One can easily see the effect of increased energy deposition in the $W25 Re$ liner when compared to the steel one. It follows from Fig. 11 that the $W25 Re$ liner provides for an overall better protection for the superconducting coils in the inner triplet. It also mitigates the local huge spike at the IP end of the Q2A quadrupole observed when using the steel liner. At the same time, the total dynamic heat load (see Fig. 12) does not vary significantly with liner because the liner is responsible mostly for an internal re-distribution of the energy deposited in the system.

The integral of the dynamic heat load is presented in Table 1. It should be noted that: (i) the data given in the second column of the Table refers to the energy deposited not only in the liner itself but also in the beam screen (see Figs. 2 and 3); (ii) in addition to the beam screen, liner, and superconducting coils, the other parts of the quadrupoles also contribute to the total heat load presented in the last column of the Table.

Since the total dynamic heat load scales with luminosity and the modifications discussed above to the quadrupoles do not give rise to significant variation, the heat load remains the outstanding constraint on the cooling system capability and the cryoplant cost. One can see from Fig. 11 that a separate cooling system for the liner, maintained at liquid nitrogen temperatures, could provide for a solution to this problem and should be studied in detail. With such a separate cooling system and a $W25 Re$ liner of increased thickness, the dynamic heat load to the superconducting coils would not exceed 20 W/m with a total heat load to the coils of 307 W.

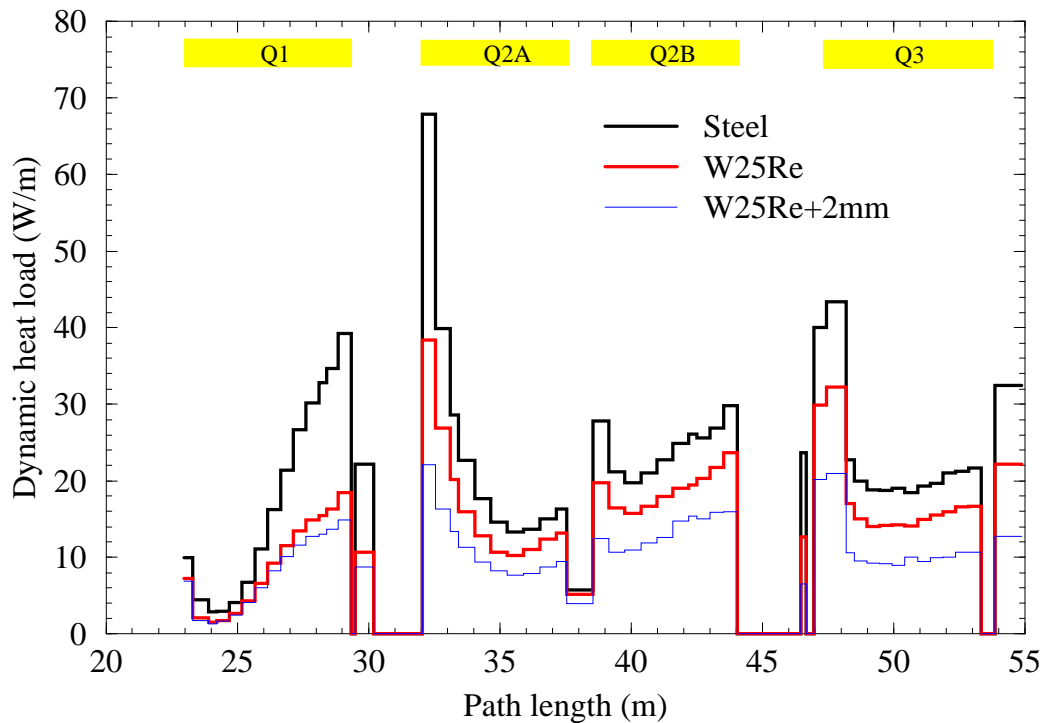
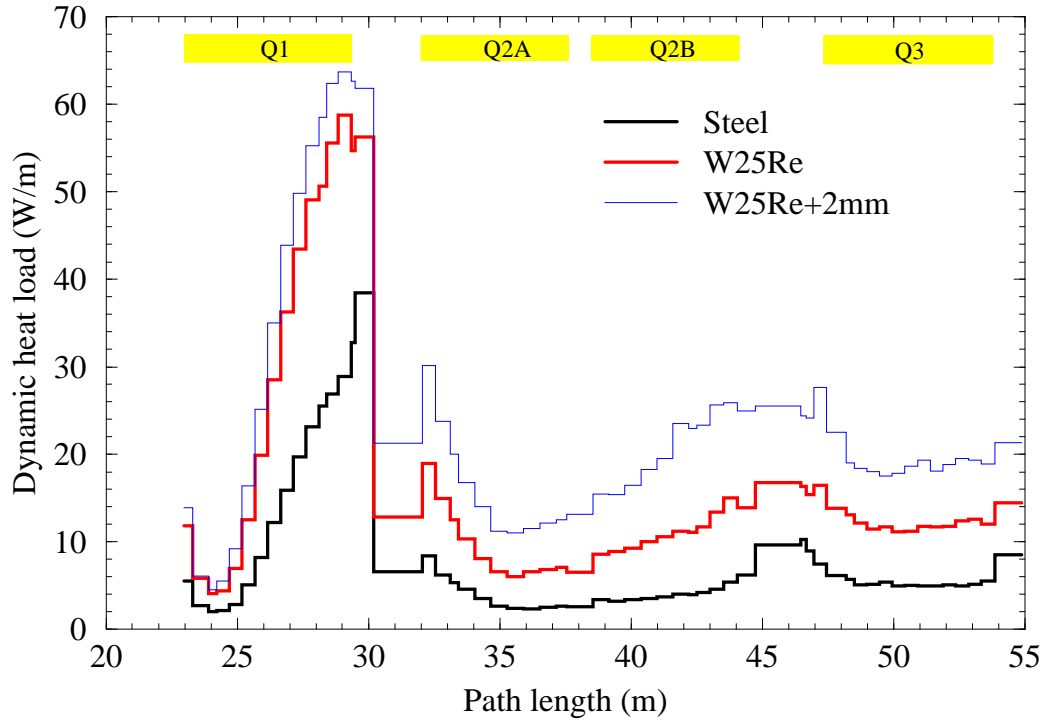


Figure 11: Dynamic heat load to the liner (top) and superconducting coils (bottom) of the 100-mm Nb_3Sn quadrupoles and correctors calculated for the steel and $W25Re$ liners of baseline thickness as well as for a $W25Re$ liner of increased thickness. $W25Re$ is used to replace both the steel liner and 1.5-mm steel cold bore adjacent to the liner (see Fig. 2).

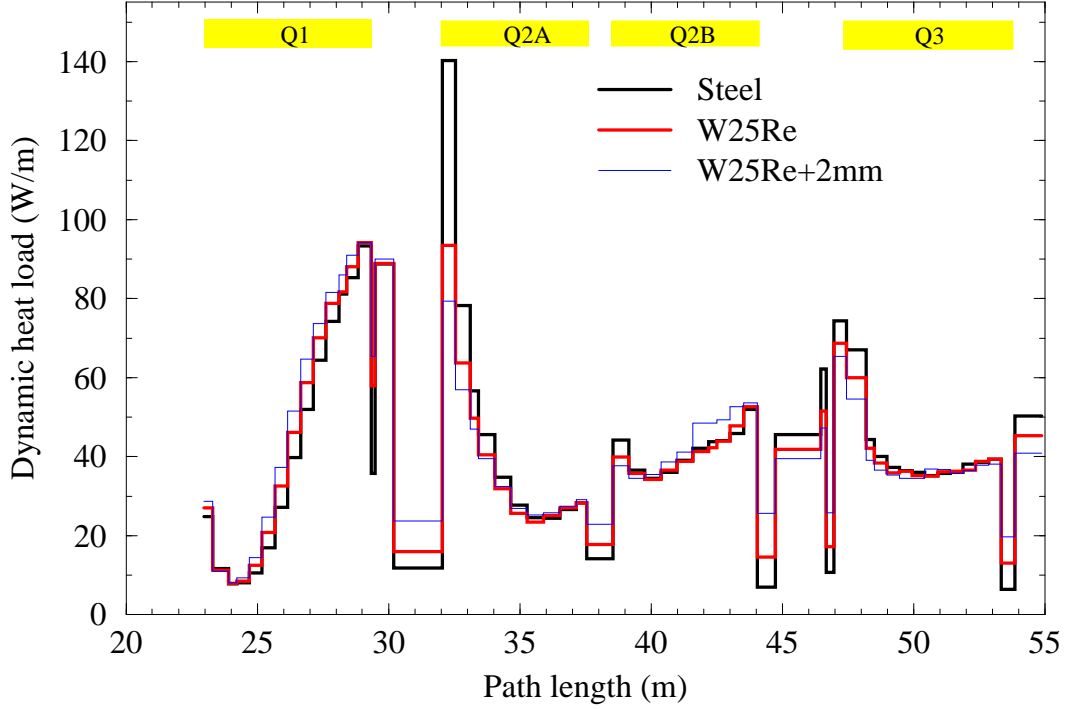


Figure 12: Distribution of total dynamic heat load in the 100-mm Nb_3Sn quadrupoles calculated for the steel and $W25Re$ liners of baseline thickness as well as for a $W25Re$ liner of increased thickness.

Table 1: Integral data on the dynamic heat load (W/m) for the inner triplet with 100-mm Nb_3Sn quadrupoles at an ultimate luminosity of $10^{35} \text{ cm}^{-2}\text{s}^{-1}$. Steel and $W25Re$ liners of baseline thickness as well as a $W25Re$ liner of increased thickness are considered.

Component	Liner			Superconducting coil			Total heat load		
	S ^{a)}	W ^{b)}	W2 ^{c)}	S ^{a)}	W ^{b)}	W2 ^{c)}	S ^{a)}	W ^{b)}	W2 ^{c)}
Q1	81	175	203	109	56	49	268	287	304
Q2A	22	52	88	132	91	62	259	217	209
Q2B	21	60	112	134	105	74	228	225	239
Q3	35	79	127	155	117	76	280	269	261
Correctors & TASB	85	146	211	117	78	46	259	271	296
Total	244	512	741	647	447	307	1294	1269	1309

^{a)} Model with a stainless steel liner of baseline thickness.

^{b)} Model with a $W25Re$ liner of baseline thickness.

^{c)} Model with a $W25Re$ liner of increased (by 2 mm) thickness.

5 Conclusions

The calculated data on peak power density and dynamic heat load to the LHC inner triplet with Nb_3Sn quadrupoles is presented at an ultimate luminosity of $10^{35} \text{ cm}^{-2}\text{s}^{-1}$. In order to reduce the peak power density to an acceptable level, various options were studied: (i) increasing inner coil diameter (90, 100, and 110 mm); (ii) increasing thickness of the inner absorber (liner); (iii) replacing the material of the liner with a tungsten-based alloy (*W25 Re*) instead of stainless steel; (iv) using spacers in the hottest spots of the SC coils. A *W25 Re* liner of increased thickness (7.2 mm in the Q1 region and 1 mm from Q2A through Q3) provides for the most effective shielding and allows us to reach the design goal of 1.7 mW/g for the 100-mm Nb_3Sn quadrupoles. The calculated total dynamic heat load to the inner triplet is about 1300 W. In order to cope with the heat load at that level, a separate cooling system for the inner absorber, maintained at liquid nitrogen temperatures, might be required.

6 Acknowledgements

The authors are thankful to Chuck Brown for useful comments.

References

- [1] N. Andreev *et al.*, IEEE Trans. Appl. Supercon., v. 11, No. 1, March 2001, p. 1558.
- [2] N.V. Mokhov, I.L. Rakhno, J.S. Kerby, J.B. Strait, "Protecting LHC IP1/IP5 Components Against Radiation Resulting from Colliding Beam Interactions", Fermilab-FN-732 (2003); LHC Project Report 633, CERN (2003).
- [3] J.B. Strait, M. Lamm, P. Limon *et al.*, "Towards a New LHC Interaction Region Design for a Luminosity Upgrade", PAC2003 Proc., p. 42; Fermilab-Conf-03/098 (2003), LHC Project Report 643 (2003).
- [4] J.B. Strait, N.V. Mokhov, T. Sen, "Overview of Possible LHC IR Upgrade Layouts", Fermilab-Conf-05/007-AD-E-T (2005).
- [5] T. Sen, J. Strait, A. V. Zlobin, Proc. 2001 Part. Accel. Conf., Chicago, June 2001, p. 3421.
- [6] N.V. Mokhov, D.R. Chichili, S.A. Gourlay *et al.*, "Superconducting Magnets in High-Radiation Environment at Supercolliders", Fermilab-Conf-06/244-AD (2006).
- [7] T. Sen, V.V. Kashikhin, P. Limon *et al.*, "Beam Physics Issues for a Possible 2nd Generation LHC IRs", *Proc. of EPAC 2002 Conf.*, Paris, pp. 371-373 (2002).
- [8] N.V. Mokhov, "The Mars Code System User's Guide", Fermilab-FN-628 (1995); N.V. Mokhov, K.K. Gudima, C. James *et al.*, "Recent enhancements to the MARS15 code", Radiation Protection Dosimetry, v. 116, pp. 99-103 (2005), Fermilab-Conf-04/053 (2004); <http://www-ap.fnal.gov/MARS/>.
- [9] A.V. Zlobin, Private communication, Fermilab (2006).
- [10] V.V. Kashikhin, Private communication, Fermilab (2002).
- [11] <http://physics.nist.gov/PhysRefData/>.

[12] <http://www.matweb.com/>.